

Paper 0

J. van Irsel¹, K. A. Lynch¹, A. C. Mule¹, M. Zettergren²

¹Department of Physics and Astronomy, Dartmouth College, Hanover, NH, 03755 USA

²Physical Sciences Department, Embry-Riddle Aeronautical University, Daytona Beach, FL, 32114 USA

Key Points:

- enter point 1 here
- enter point 2 here
- enter point 3 here

9 **Abstract**
10 Enter your Abstract here

11 **Plain Language Summary**

12 Enter your Plain Language Summary here or delete this section.

13 **1 Introduction**

14 **1.1 Motivation**

15 **What does this paper provide and why?** Measurements of auroral arc systems are
16 often sparse, heterogeneous, and distributed, yet ionospheric models generally require
17 continuous 2D input drivers. Moreover, the distribution is commonly no more than one,
18 maybe two sets of dense across-arc data tracks leaving little to no information on along-
19 arc morphologies. Luckily, information about these morphologies is something that all-
20 sky imagery can provide.

21 This paper outlines three empirical methods for creating electrostatic, continuous,
22 2D, topside F-region boundary conditions from distributed optical data provided by all-
23 sky, multi-spectral imagery and plasma flow data tracks provided by spacecraft, sound-
24 ing rockets and/or radar measurements. These methodologies focus on typical sheet-like
25 discrete auroral arc structures with high across- to along-arc gradient ratios. Further-
26 more, this paper looks at the use of these boundary conditions in driving and assessing
27 3D auroral ionospheric simulations.

28 **Why do we care about 3D auroral ionospheric simulations?** The understanding of
29 auroral arc scale science plays an important role in interpreting magnetosphere-ionosphere
30 (MI) coupling, the ionospheric end of which itself involves complex, system level science
31 which is ongoing (Wolf, 1975; Seyler, 1990; Cowley, 2000; Lotko, 2004; Fujii et al., 2011,
32 2012; Marghitu, 2012; Khazanov et al., 2018; Clayton et al., 2019, 2021; Yano & Ebihara,
33 2021; Lynch et al., 2022; Enengl et al., 2023; Wang et al., 2024). MI coupling de-
34 mands self-consistent, topside maps of field-aligned current (FAC) and convection plasma
35 flow that agree with a 3D ionospheric conductivity volume created by charged particle,
36 auroral precipitation. This is why the auroral ionosphere plays a non-passive role in this
37 coupling. At high latitudes, the 2D topside relation between quasi-static convective flow,
38 FAC, and conductances is (Kelley, 2009, Eq. 8.15):

$$j_{\parallel}(x, y) = \Sigma_P \nabla_{\perp} \cdot \mathbf{E} + \mathbf{E} \cdot \nabla_{\perp} \Sigma_P + (\mathbf{E} \times \mathbf{b}) \cdot \nabla_{\perp} \Sigma_H, \quad (1)$$

39 where j_{\parallel} is the topside map of FAC orthogonal to the local magnetic field, $\Sigma_{P,H}$ are the
40 height-integrated Pedersen and Hall conductivities, i.e. conductances, \mathbf{E} is the ionospheric
41 electric field, and $\mathbf{b} = \mathbf{B}/B$ is the magnetic field direction. This explains, in the ab-
42 sence of strong dynamics, how magnetospheric currents and convection patterns couple
43 to the ionosphere given 2D conductance maps. However, this perspective ignores the re-
44 active effects of the ionosphere and, in fact, it integrates out all altitudinal dependen-
45 cies. E.g. finite, altitude dependent recombination times in combination with plasma trans-
46 port can produce complex 3D electron density structures providing an auroral precip-
47 itation hysteresis in conductance maps. Moreover, the 3D conductivity volume is highly
48 sensitive to auroral precipitation by means of impact ionization. In particular, the pre-
49 cipitation energy spectra determine ionization rate profiles that are altitude dependent
50 (Fang et al., 2008, 2010). This is why it is important to study the full 3D picture of au-
51 roral system science. This is done by looking at FAC closure influenced by auroral pre-
52 cipitation in a way that is both geophysical and self-consistent with plasma convection.
53 To do this, we need 3D ionospheric simulations which require continuous 2D input drivers.

54 **1.2 Background**

55 **Nicolls 2014 and Bristow 2016.** Nicolls et al. (2014) undertake the mapping (or “imaging”)
 56 of 2D electric field distributions using line-of-sight (LOS) radar plasma flow mea-
 57 surements. They outline a regularized least-squares fitting algorithm which takes direct
 58 LOS flow measurements along with their measurement error and produces a 2D electric
 59 potential map. This is a difficult feat in that a single LOS measurement only carries in-
 60 formation on one component of the electric field; it requires multiple beams to discover
 61 information about the full vector field. Part of their regularization minimizes the mean
 62 squared curvature of the potential field (with a personal tailoring parameter) which re-
 63 sults in the smoothest possible solutions and minimizes gradients isotropically, something
 64 not well suited for sheet-like auroral arcs.

65 Bristow et al. (2016) approach the same problem differently using Local Divergence-
 66 Free Fitting (LDFF). They impose the local constraint of divergence-free plasma con-
 67 vection and treat this in the same way the recomposition of two LOS measurements con-
 68 straint is treated. This achieves larger gradients, and in turn higher spatial resolution,
 69 but this is still indiscriminate to along- or across-arc directions.

70 **Lompe, AMIE, and KRM.** Laundal et al. (2022) describe methodology for the Lo-
 71 cal mapping of polar ionospheric electrodynamics (Lompe). This is an assimilative tool
 72 that gathers relatively dense, heterogeneous observational data provided by ground/space
 73 magnetometers, optical all-sky observatories, and radars, and performs a local/regional
 74 mapping of the polar ionospheric electrodynamics. They point out that they use Spher-
 75 ical Elementary Current Systems (SECS) (Amm, 1997) instead of the more global spher-
 76 ical bases used by other assimilative tools like the Kamide-Richmond-Matsushita (KRM)
 77 (Kamide et al., 1981) and the Assimilative Mapping of Ionospheric Electrodynamics (AMIE)
 78 (Richmond & Kamide, 1988) methods, which allows more flexibility when it comes to
 79 spatial scales.

80 **Clayton method.** This paper includes a formalization of techniques developed dur-
 81 ing the phase A Concept Study Report (CSR) for the Auroral Reconstruction CubeSwarm
 82 (ARCS) mission proposal (Lynch et al., 2024; Erlandson et al., 2024) as well as a con-
 83 tinuation of techniques developed by Clayton et al. (2019, 2021) with several improve-
 84 ments. We outline methodologies for the continuous mapping of plasma flow data tracks
 85 which focus on auroral physical and gradient scale lengths, and discrete sheet-like mor-
 86 phologies.

87 **1.3 Outline.**

88 Section 2 describes the reconstruction, replication, and weighted replication method-
 89 ology along with an example usages of each one. Section 3 outlines and compares two
 90 example 3D auroral multi-fluid simulations driven by plasma flow maps derived by the
 91 replication method in Section 2.2. In section 4 we discuss our results and outline how
 92 we intend to use these methods in future work and we conclude this work in Section 5.

93 **2 Methodologies**

94 We outline three methods for developing continuous plasma flow maps from lim-
 95 ited remote sensed or in situ flow data tracks. Section 2.1 outlines the first methodol-
 96 ogy coined “reconstruction”, which stems from science section in the ARCS CSR (Lynch
 97 et al., 2024). This report proposes an arrayed constellation of spacecraft spanning both
 98 multiple latitudes *and* longitudes, i.e. a “CubeSwarm”. The reconstruction method pri-
 99 oritizes accurate flow representation interior to the constellation array and builds the
 100 flow map using a set of electric potential ridges, ensuring electrostatic flow. These ridges
 101 follow some definition of a single auroral arc boundary determined using morphological

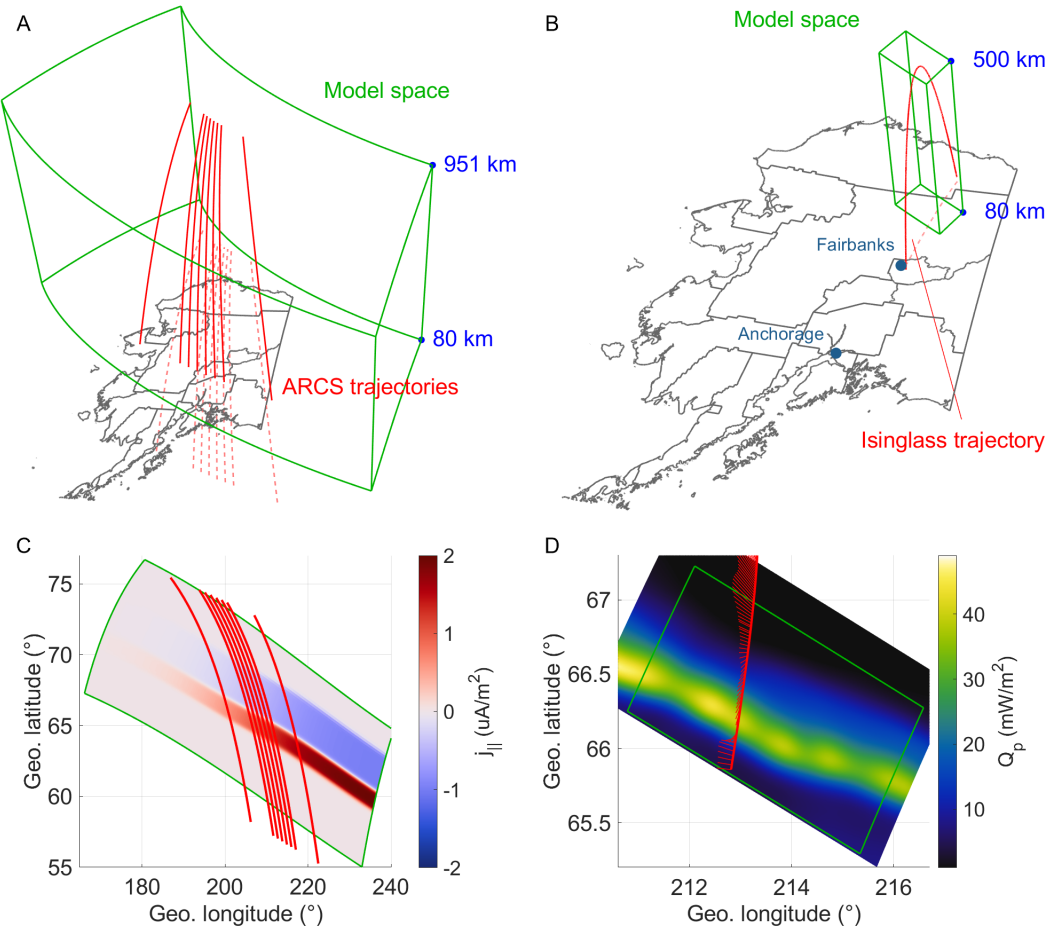


Figure 1. Context relating to the simulations used in demonstrating the reconstruction and replication methods. **A:** The simulation model space (green) and the ARCS trajectories (red) in reference to Alaska. **B:** Same as panel A but with the Isinglass trajectory. **C:** 2D FAC input map in reference to the model space (green). **D:** Total precipitating energy flux and plasma flow data in reference to the model space (green).

features of all-sky, multi-spectral imagery. The left column of Figure 1 outlines the context of the Observing System Simulation Experiment (OSSE) used to demonstrate the reconstruction technique. This OSSE is interpolated with virtual spacecraft to provide fictitious plasma flow data.

The second method, “replication”, outlined in Section 2.2, stems from similar methodology outlined by Clayton et al. (2019, 2021) who use data from the Isinglass sounding rocket campaign P.I. K. A. Lynch in conjunction with imagery from the UAF Geophysical Institute’s Poker Flat Digital All-Sky Camera (DASC) [dasc data ref](#). This method makes use of plasma flow data from a single crossing, whether from a sounding rocket (Clayton et al., 2019, 2021), spacecraft [swarm data ref](#) [tii aurora archer maybe](#), or mesoscale radar [pfisr ref](#) [recent aurora](#). Here, the data are replicated, scaled, and rotated in accordance with *two* auroral arc boundaries, again, determined through all-sky imagery features. The right column of Figure 1 shows the context of the simulation used to demonstrate the replication technique.

The third method, a permutation of the second named “weighted replication”, is outlined in Section 2.3 and uses two (or more) tracks in conjunction with the all-sky imagery. This method repeats part of the replication methodology for each track and performs a weighted averaging on the interpolated flow maps (prior to enforcing electrostatics) with the weighting being based on the geometric distances to either track.

In all three methods, one of the main difficulties in creating a continuous plasma flow map lies in the constraint that it is divergence-less, i.e. electrostatic (Ruohoniemi et al., 1989; Nicolls et al., 2014). Vector fitting algorithms exist which handle this constraint, but will often provide large vortices to act as sources/sinks, replacing points of divergence/convergence [refs](#).

2.1 Reconstruction

This section provides a proof-of-concept reconstruction using an OSSE used by Lynch et al. (2024) in where a localized “CubeSwarm” of virtual spacecraft scrape data from a 3D auroral arc simulation as they orbit through (see Figure 1A). The simulation used in this section is data inspired, but idealized; it is driven with a single pair of FAC sheets that have a slight bend in their profile and fade westward from ± 1 to $0 \mu\text{A}/\text{m}^2$ over the span of the model space (see Figure 1C). The precipitation input maps are of a similarly shaped arc embedded within the poleward FAC sheet peaking at an energy flux of $3 \text{ mW}/\text{m}^2$ and characteristic energy of 3 keV with gradient scale lengths of 40 km.

2.1.1 Reconstruction algorithm

With hindsight into what the form of the electric potential map is, and to avoid large plasma flow vortices, we construct the potential map out of a sum a user-defined number, N_k , of pseudo-basis functions each governed by a set of parameters. The functional form of each of them is an inclined Gaussian ridge, i.e. a Gaussian profile northward that extrudes east- and westward with a constant sloped amplitude, while following the boundary of the arc. This is done to find potential solutions that priorities across-arc gradients while remaining relatively unstructured along the arc. The $\mathbf{E} \times \mathbf{B}$ plasma flow derived from this potential field is then compared against the virtual plasma flow data and their mean square differences are then minimized over the parameter space.

The arc boundary is determined using standard Sobel edge detection (Sobel, 2014). Given the idealistic nature of the OSSE used in demonstrating this method, this suffices, but we want to caution the reader regarding the complexities of determining less ideal arc boundaries. In any case, after determining an appropriate set of boundary points, they are least-squares fit against the following functional form:

$$b(x; \bar{A}) = \sum_{j=1}^{N_j} \left[A_{j1} + A_{j2} \tanh\left(\frac{x - A_{j3}}{A_{j4}}\right) \right], \quad (2)$$

with \bar{A}^0 being the $N_j \times 4$ best fitting boundary parameter matrix, N_j the user-defined number of summation terms, and x the linear magnetic east coordinate. The choice of summing hyperbolic tangents lies in the tendency of auroral arcs to be aligned magnetic east-west and relatively unstructured in this direction.

With this, we define our pseudo-basis potential ridge as

$$\phi_k(\mathbf{r}; \bar{P}, \bar{A}) = (P_{k1}x + P_{k2}) \exp\left[-\frac{(y - P_{k3} - b(x; \bar{A}))^2}{P_{k4}^2}\right], \quad (3)$$

155 where \bar{P} is the $N_k \times 4$ potential parameter matrix and y being the linear magnetic north
156 coordinate, giving a total potential field of

$$\phi(\mathbf{r}; \bar{P}, \bar{A}) = \sum_{k=1}^{N_k} \phi_k(\mathbf{r}; \bar{P}, \bar{A}). \quad (4)$$

157 Prior work by [ref tucker](#) aimed to instead warp the flow field via a coordinate transfor-
158 mation to along/across-arc coordinates, similar to those used by Marghitu (2012), but
159 we have found the solution used here to be both simpler to implement and faster.

160 The plasma flow data from the virtual spacecraft provide the vectors $\mathbf{v}_i = (v_{xi}, v_{yi})$
161 at positions $\mathbf{r}_i = (x_i, y_i)$ with i being the sample number. Generally, this flow data would
162 require some mindful Gaussian smoothing, but more on this in Section [s:caution](#). With
163 this, the electric field components to be compared against the plasma flow data are

$$\begin{aligned} E'_x(\mathbf{r}_i; \bar{P}, \bar{A}) &= -\frac{\partial}{\partial x} \phi(\mathbf{r}; \bar{P}, \bar{A}) \Big|_{\mathbf{r}_i} \\ &= -\sum_{k=1}^{N_k} \left[P_{k1} + \frac{2\gamma(\mathbf{r}_i; \bar{P}, \bar{A})}{P_{k4}^2} (P_{k1}x_i + P_{k2}) \frac{\partial b}{\partial x} \Big|_{x_i} \right] \exp \left[-\frac{\gamma(\mathbf{r}_i; \bar{P}, \bar{A})^2}{P_{k4}^2} \right] \end{aligned} \quad (5)$$

$$\begin{aligned} E'_y(\mathbf{r}_i; \bar{P}, \bar{A}) &= -\frac{\partial}{\partial y} \phi(\mathbf{r}; \bar{P}, \bar{A}) \Big|_{\mathbf{r}_i} \\ &= \sum_{k=1}^{N_k} \frac{2\gamma(\mathbf{r}_i; \bar{P}, \bar{A})}{P_{k4}^2} (P_{k1}x_i + P_{k2}) \exp \left[-\frac{\gamma(\mathbf{r}_i; \bar{P}, \bar{A})^2}{P_{k4}^2} \right], \end{aligned} \quad (6)$$

164 with $\gamma(\mathbf{r}; \bar{P}, \bar{A}) = y - P_{k3} - b(x; \bar{A})$ and

$$\frac{\partial b}{\partial x} = \sum_{j=1}^{N_j} \frac{A_{j2}}{A_{j4}} \operatorname{sech}^2 \left(\frac{x - A_{j3}}{A_{j4}} \right). \quad (7)$$

165 From here, with $\mathbf{B} = -B\hat{z}$ and z the linear magnetic up coordinate, we rotate the elec-
166 tric field providing plasma flow:

$$\mathbf{v}'(\mathbf{r}; \bar{P}, \bar{A}) = (v'_x, v'_y, 0) = \frac{\mathbf{E}' \times \mathbf{B}}{B^2} = \frac{1}{B} (-E'_y, E'_x, 0). \quad (8)$$

167 This reduces the problem to finding the parameter matrix, \bar{P}^0 , which solves

$$\min_{\bar{P}} \sum_i [(v'_x(\mathbf{r}_i; \bar{P}, \bar{A}^0), v'_y(\mathbf{r}_i; \bar{P}, \bar{A}^0)) - (v_{xi}, v_{yi})]^2, \quad (9)$$

168 such that, with the optimized parameter matrix, the continuous plasma flow map is given
169 by

$$\mathbf{v}_c(\mathbf{r}) = \mathbf{v}'(\mathbf{r}; \bar{P}^0, \bar{A}^0) \quad (10)$$

170 and subsequently the continuous potential map used to drive ionospheric models is

$$\phi_c(\mathbf{r}) = \phi(\mathbf{r}; \bar{P}^0, \bar{A}^0). \quad (11)$$

171 By using the potential ridges, we prioritize solutions for ϕ_c that have sheet-like morphol-
172 ogy in contrast to what has been done before (Kamide et al., 1981; Amm, 1997; Nicolls
173 et al., 2014; Bristow et al., 2016; Laundal et al., 2022).

174 2.1.2 Reconstruction example

175 Figure 2 shows an example usage of the reconstruction algorithm. This example
176 was developed for ARCS (Lynch et al., 2024) to verify the ability of plasma flow recon-
177 struction given a local grouping of spacecraft. The virtual orbits are arranged densely
178 to be able to provide map of along- and across-arc gradients.

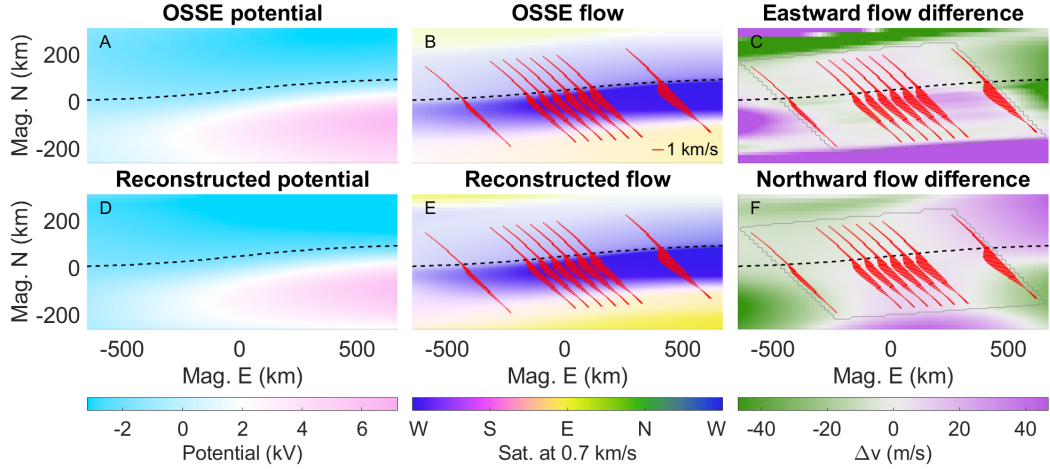


Figure 2. Example of a plasma flow field reconstruction. **A:** The electric potential map used to drive the OSSE with the boundary, b , overlaid. **B:** The resulting flow field with the virtual flow data points (red), \mathbf{v}_i , interpolated from it. The color representation of flow has the direction depicted by hue and the intensity by the color saturation. **D, E:** The reconstructed electric potential and flow. **C, F:** The difference between the reconstructed and OSSE east- and northward flow.

The black dashed lines are the imagery derived boundary, b , and the bag of plasma flow vectors, \mathbf{v}_i , is overlaid in red. The reconstructed electric potential, ϕ_c , and reconstructed flow, \mathbf{v}_c , match well within the spacecraft region (gray outline in Fig. 2C, F) as per design. The maximum absolute flow difference in this region is 47 m/s eastward and 28 m/s northward with averages of 5(12) and 5(8) m/s. Outside the region, however, the error quickly ramps up due to the under-regulated potential ridge parameters, \bar{P} .

2.1.3 Possible improvements

Note about how we're moving on from this, but here are possible improvements one could do. Proper regularization on the potential ridges, ϕ_k , can be used to stretch the region of good fit as presently the goodness-of-fit rapidly decreases when moving out of the spacecraft region. Furthermore, the electric field resulting from a single ridge i.e. Eqs. (5-6), far from the fitting region is

$$\lim_{\mathbf{r} \rightarrow \infty} E_{xk}(\mathbf{r}; \bar{P}, \bar{A}) = -P_{k1} \exp \left[-\frac{(y - P_{k3} - b_{\pm\infty})^2}{P_{k4}^2} \right] \quad (12)$$

$$\lim_{\mathbf{r} \rightarrow \infty} E_{yk}(\mathbf{r}; \bar{P}, \bar{A}) = \frac{2}{P_{k4}^2} (P_{k1}x + P_{k2})(y - P_{k3} - b_{\pm\infty}) \exp \left[-\frac{(y - P_{k3} - b_{\pm\infty})^2}{P_{k4}^2} \right], \quad (13)$$

where $b_{\pm\infty} = \sum_j (A_{j1} \pm A_{j2})$ and $\partial b / \partial x (x \rightarrow \pm\infty) \rightarrow 0$. Clearly, E_{xk} remains finite, but E_{yk} diverges as $|y| < \infty \wedge x \rightarrow \infty$. Granted we work within the bounds of the model space, but slowing down this divergence would aid in regularization and smoother solutions. In actuality, models often require a good amount of buffer surrounding the region of interest into which the flow map needs to extrapolate. Lastly, incorporating weighted fitting would provide error estimates for reconstructions from real data as opposed to an OSSE, e.g. weights of $w_i = 1/\sigma_i^2$ with σ_i being instrument error assuming a diagonal measurement covariance matrix.

201 **2.2 Replication**

202 The second method of developing continuous plasma flow maps uses plasma flow
 203 data with approximately across-arc tracks in conjunction with all-sky, multi-spectral im-
 204 agery. In this method, data is replicated along-arc using direct and indirect information
 205 from the imagery. Primary *and* secondary boundaries are determined along which the
 206 track data is translated, scaled, and the flow data is rotated to be tangent with the pri-
 207 mary boundary. The example used here uses data set “c5” from Clayton et al. (2021).

208 **2.2.1 Arc boundary definitions**

209 Determining the arc boundaries from multi-spectral imagery data firstly requires
 210 an inversion (ref) to a map of total energy flux, Q_p , and characteristic energy, E_p , of the
 211 precipitating electrons. From these a proxy for the Pedersen conductance is made which,
 212 at the time of writing, is done using Eq. (3) by Robinson et al. (1987):

$$\Sigma_P(x, y) = \frac{40(E_p(x, y)/\text{keV})}{16 + (E_p(x, y)/\text{keV})^2} \left(Q_p(x, y)/\text{mW/m}^2 \right)^{1/2}. \quad (14)$$

213 The reader is cautioned, however, to use multi- and/or two-stream transport mod-
 214 els, such as the GLobal airglOW (GLOW) model (Solomon, 2017), or look-up tables gen-
 215 erated by such models, to determine a more accurate Pedersen conductance.

216 With this, the primary and secondary arc boundaries are established in one of two
 217 ways on *either* the total energy flux *or* Pedersen conductance: 1) finding the magnetic
 218 latitude of the first two most prominent edges at each magnetic longitude using Sobel
 219 edge detection (Sobel, 2014) in the magnetic northward direction, or 2) following a con-
 220 tour line at two isovalues which can be chosen directly, or determined at the locations
 221 of the central two most prominent edges along the track. *In either case, the boundary*
 222 *is Gaussian smoothed. should we do this? Is it harder to find a laminar flow solution with*
 223 *less smoothing? Is there an anti-correlation to curliness and boundary smoothing? Do*
 224 *more wiggly arcs have more hall closure, or is the penalty more curl of A?* Figure 3 shows
 225 the Pedersen conductance and its magnetic northward Sobel convolution along with the
 226 primary and secondary boundaries determined using method 2 with Pedersen conduc-
 227 tance and method 1 with total energy flux. In the remainder of this paper, we use bound-
 228 aries determined using Pedersen conductance contour lines.

229 **2.2.2 Flow data replication**

230 Firstly, the plasma flow data track is Gaussian smoothed (more on this in Section
 231 ref section) and, prior to doing any replication, we split the flow field into two compo-
 232 nents: 1) the background flow treated as a constant, large-scale, global disturbance, and
 233 2) the small-scale disturbances imposed by the arc itself:

$$\mathbf{v}(\mathbf{r}) = \mathbf{v}_{\text{arc}}(\mathbf{r}) + \mathbf{v}_{\text{bg}}. \quad (15)$$

234 In absence of background flow, the most basic model of an auroral arc is composed
 235 of only across-arc flow shear, i.e. electric field shocks (Marghitu, 2012). Thus, we define
 236 the background flow such that, once removed, the flow at the intersection of the track
 237 and the primary boundary is tangent to that boundary. Furthermore, this simplistic model
 238 has the arc defined as a band of enhanced conductance in which we expect the electric
 239 field to quench. Thus, it makes sense to replicate this data along the arc boundaries, while
 240 remaining tangent to it, and scaling such that the shorted out electric fields remain in-
 241 side the area of enhanced conductance. This leads to the following plasma flow data track
 242 replication algorithm:

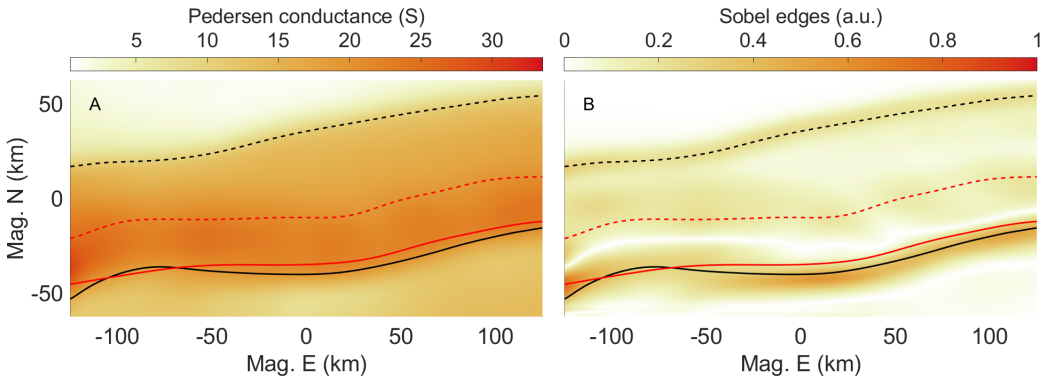


Figure 3. Primary (solid) and secondary (dashed) boundaries using Pedersen conductance and contour lines at 19.1 S and 10.5 S (black). In red are the boundaries determined using the energy flux (not shown) with the steepest gradient method. **A:** Pedersen conductance determined via Eq. (14). **B:** Magnetic northward Sobel convolution of the Pedersen conductance. Both sets of boundaries have an approximate smoothing window of 15 km.

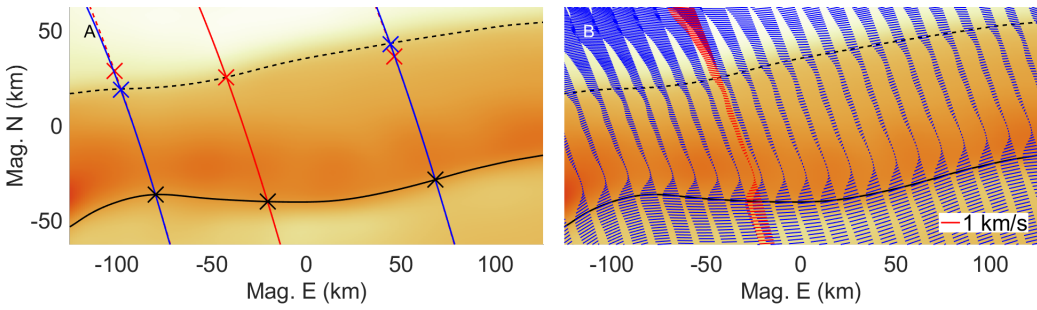


Figure 4. In situ trajectory flow data replication overlaid on the same conductance map from Figure 3A. **A:** Two example replications (blue) of the original trajectory (red) along the primary arc boundary (solid black). The black crosses have the same flow data. The red/blue crosses indicate flow data before/after scaling to meet up with the secondary arc boundary (dashed black). **B:** A low density replication (blue) along with the original, smoothed flow data (red).

- 243 1. The original track is translated by some amount following the primary arc bound-
244 ary such that the original and replicated flow data are equal at the primary boundary-
245 track intersections.
246 2. The replicated track is scaled in the along-track direction such that the original
247 and replicated flow data are equal at the secondary boundary-track intersections.
248 3. The flow data of the replicated track is rotated by a constant angle per track such
249 that it remains to be tangent to the primary arc boundary.
250 4. Repeat this replication for multiple translations along the arc until the 2D model
251 space is filled with a replication rate higher than the eastward Nyquist spacing.

252 Figure 4 illustrates these steps given the boundaries of Figure 3. The left panel shows
253 two examples of how replications of the original trajectory are translated and scaled. The
254 western replication example is scaled down to have the data at the red cross meet the
255 secondary boundary, while the eastern replication is scaled up to do the same. The right
256 panel shows the replication, but done only for a few instances for illustration purposes.
257 This also shows the rotated flow vectors keeping tangent with the primary boundary.

258 **2.2.3 Enforcing electrostatic flow**

259 Next, the replicated flow data is interpolated onto the model grid. This section out-
 260 lines three choices of fitting an electric potential map to this interpolated flow field, $\mathbf{v}_{\text{arc}} =$
 261 $\mathbf{E}_{\text{arc}} \times \mathbf{B} / B^2$, where \mathbf{B} is the magnetic field from Eq. (8) and \mathbf{E}_{arc} is the arc disturbed
 262 ionospheric electric field perpendicular to \mathbf{B} . The interpolated flow fields' associated elec-
 263 tric field reads as follows:

$$\mathbf{E}_{\text{arc}}(\mathbf{r}) = -\mathbf{v}_{\text{arc}}(\mathbf{r}) \times \mathbf{B} = \mathbf{E}_I(\mathbf{r}) + \mathbf{E}_S(\mathbf{r}) = -\nabla\phi_c(\mathbf{r}) + \nabla \times \mathbf{A}(\mathbf{r}), \quad (16)$$

264 where ϕ_c is the electric potential map we're looking for and \mathbf{A} is the magnetic vector po-
 265 tential. We want to remove the non-electrostatic part, i.e. find the irrotational electric
 266 field, \mathbf{E}_I , and remove the solenoidal field, \mathbf{E}_S , in a way that best agrees with the inter-
 267 polated flow field. Three choices of doing so are as follows:

- 268 1. **Brute force:** Perform a least-squares fitting algorithm (Levenberg–Marquardt
 269 in our case) that directly fits a potential map, ϕ , i.e.

$$\min_{\phi} \|\nabla \times \mathbf{A}(\mathbf{r})\|_2^2 = \min_{\phi} \|\nabla\phi(\mathbf{r}) + \mathbf{E}_{\text{arc}}(\mathbf{r})\|_2^2 = \min_{\phi} \sum_{i,j} \left((\nabla\phi)_{ij} + \mathbf{E}_{\text{arc},ij} \right)^2, \quad (17)$$

270 the solution of which, ϕ_c , is the continuous potential map.

- 271 2. **Averaged path-integrated:** Average several path-integrated potential maps in
 272 an attempt to drown out the non-conservative part of the interpolated field, i.e.

$$\phi_l(\mathbf{r}) = \int_{x_l}^x dx' \mathbf{E}_{\text{arc}}(x', y_l) \cdot \hat{x} + \int_{y_l}^y dy' \mathbf{E}_{\text{arc}}(x, y') \cdot \hat{y}, \quad (18)$$

273 where we take $\phi_c = \langle \phi_l \rangle$.

- 274 3. **Helmholtz decomposition:** Use the Fourier transform method for Helmholtz
 275 decomposition (Mule, 2023, Pers. comm.). Taking the 2D Fourier transform of Eq. (16)
 276 gives us

$$\mathbf{G}(\mathbf{k}) = -i\mathbf{k}G_{\phi}(\mathbf{k}) + i\mathbf{k} \times \mathbf{G}_{\mathbf{A}}(\mathbf{k}), \quad (19)$$

277 where $\mathbf{k} = (k_x, k_y)$ is the wave vector and \mathbf{G} , G_{ϕ} , and $\mathbf{G}_{\mathbf{A}}$ are the Fourier trans-
 278 forms of \mathbf{E}_{arc} , ϕ_c , and \mathbf{A} respectively. Taking the dot product of Eq. (19) with \mathbf{k}
 279 gives us an expression for the Fourier transform of the potential:

$$G_{\phi}(\mathbf{k}) = i \frac{\mathbf{k} \cdot \mathbf{G}(\mathbf{k})}{\|\mathbf{k}\|^2}, \quad (20)$$

280 such that

$$\phi_0(\mathbf{r}) = \mathcal{F}^{-1}\{G_{\phi}(\mathbf{k})\} = \int_{-\infty}^{+\infty} dk_x \int_{-\infty}^{+\infty} dk_y G_{\phi}(\mathbf{k}) e^{i(xk_x + yk_y)}. \quad (21)$$

281 Here we've found the electric potential up to a harmonic function (i.e. gauge in-
 282 variance). The potential map we want is $\phi_c = \phi_0 + f$ where $\nabla^2 f = 0$. One choice
 283 of f has the average electric field remain the same such that

$$f_a(\mathbf{r}) = \langle -\nabla\phi_0(\mathbf{r}) - \mathbf{E}_{\text{arc}}(\mathbf{r}) \rangle \cdot \mathbf{r}. \quad (22)$$

284 A second option for f solves the optimization problem

$$\min_{\bar{F}} \left\| -\nabla(\phi_0(\mathbf{r}) + f_b^m(\mathbf{r}; \bar{F})) - \mathbf{E}_{\text{arc}}(\mathbf{r}) \right\|_2^2 \quad \text{with } \mathbf{r} \in \mathcal{M}, \quad (23)$$

285 where \bar{F} is an $m \times 2$ parameter matrix, \mathcal{M} is a user defined masking domain sur-
 286 rounding the primary and/or secondary boundary, and original track, and f_b^m is

the most general m order polynomial in x and y that satisfies Laplace's equation:

$$f_b^m(\mathbf{r}; \bar{F}) = \sum_{n=1}^m \sum_{q=0}^{\lfloor n/2 \rfloor} (-1)^q \left[\frac{F_{n1}}{\rho^{n-1}} \binom{n}{2q+1} x^{2q+1} y^{n-2q-1} + \frac{F_{n2}}{\rho^{n-1}} \binom{n}{2q} x^{2q} y^{n-2q} \right], \quad (24)$$

where ρ is a regularization parameter balancing higher order terms. To show this is the most general case, take the complex polynomial of degree m

$$p(z) = \sum_{n=0}^m F_n^* z^n, \text{ where } z^n = (x + iy)^n = \sum_{q'=0}^n \binom{n}{q'} x^{q'} (iy)^{n-q'}, \quad (25)$$

and recognize that the homogeneous polynomial z^n is analytic which therefore has harmonic real and imaginary parts (Ahlfors, 1953). This gives two parameters, the real and imaginary parts of F_n^* , for each value of n . To show uniqueness, we recognize that the Laplacian maps homogeneous polynomials of degree n to those of degree $n-2$, the domain and image of which have dimensions n and $n-2$ respectively. By the rank nullity theorem (Mule, 2024, Pers. comm.), this means the dimension of the kernel of the Laplacian is $n - (n-2) = 2$, so we've found all solutions. An example for $m = 2$ and $\rho = 10$ m gives

$$f_b^3(x, y, \bar{F}) = F_{11}x + F_{12}y + \frac{F_{21}}{10}(x^2 - y^2) + \frac{F_{22}}{10}xy. \quad (26)$$

Note that with q in meters and \bar{F} in V/m has f_b in volts. When solving for this optimization the initial guess is taken to be $(f_2^m)_0 = f_a$.

Along with the interpolated flow field (column 1), examples of the the brute force and Helmholtz decomposition methods are shown in Figure 5 (columns 2-3). The averaged path-integrated method is not shown as it does not perform as well, perhaps due to the accumulation of systematic error. The divergence panel shows that of the interpolated flow field and indicates the location of rotational signatures which are interpretable as Alfvénic. Although the brute force method is easiest to justify being the “best” fit, it is also by far the slowest, taking at least several hours on a clustered machine. The Helmholtz decomposition method, on the other hand, has the advantage of using the fast Fourier transform method and it compares reasonably well, even when using the direct harmonic solution, f_a . This is illustrated in Figure 6 which shows the residual between the brute force solution and the potential from Eq. (21) compared against a masked and unmasked harmonic fit. Clearly, a constant background electric field match, i.e. a harmonic function that is constant sloped plane, f_a , is a first order solution in this particular case but this requires further confirmation for other cases. The masking acts as a binary **placeholder** for a continuous instrument error based weighting map. Such an improved map will aid in constraining the potential in the corners of the model space (see Figure 6C).

reviewer Q: if brute force so slow why not use reconstructor from previous section?
Even a 4x512 parameter matrix will be much faster than 128x256 cells. reconstructor is an early version of replicator, this can (and perhaps should) be used in place of the pseudo basis technique.

2.2.4 Replication example

Figure 7 shows the replication methodology applied to the “c5” example by Clayton et al. (2021) (see their Table 1). The top row has the scaling and rotating applied, whereas the bottom row is done with neither. Firstly, the applied scaling to the replication results in a co-location of the shorted out electric field and the auroral precipitation as seen by the Σ_P contour lines in panel A, in comparison to panel D. Secondly, the applied rotation provides more streamlined plasma flow, in the literal sense, as seen by the change from southwest to west to southwest flow in panel A. In contrast, without rotation the

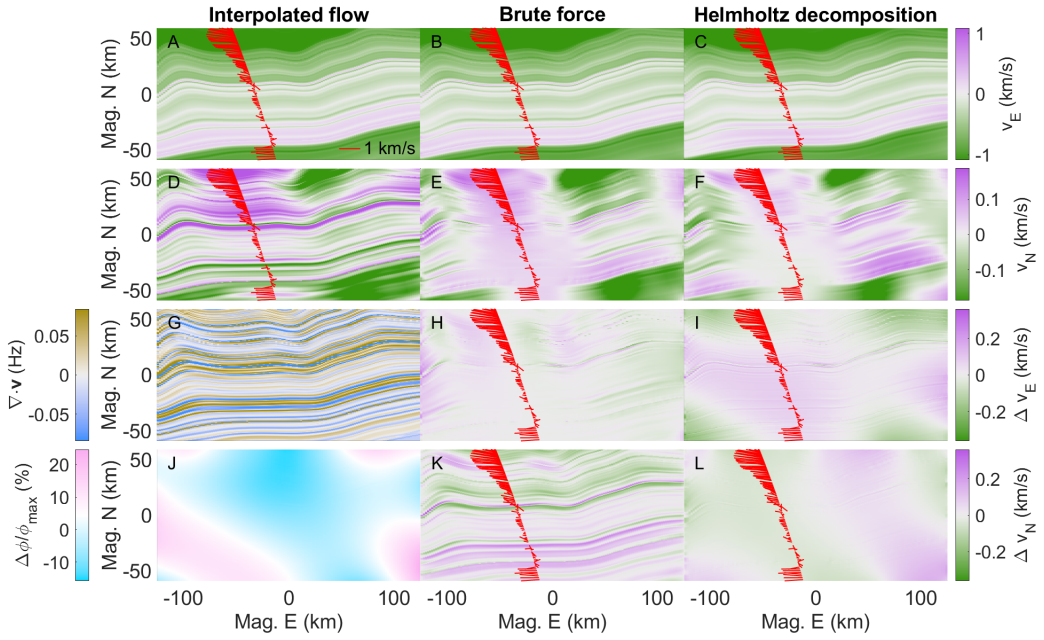


Figure 5. Comparison of fitting a potential map to an interpolated flow map, v_{arc} . **A-C:** Eastward interpolated, brute force fitted, and Helmholtz decomposed flow. **D-F:** Same but northward. **G:** Divergence of the interpolated flow. **H, K:** Difference in east and northward flow between brute force and interpolated. **I, L:** Difference in east and northward flow between Helmholtz decomposed and brute force. **J:** Relative difference in potential between brute force and Helmholtz decomposed. Needed?

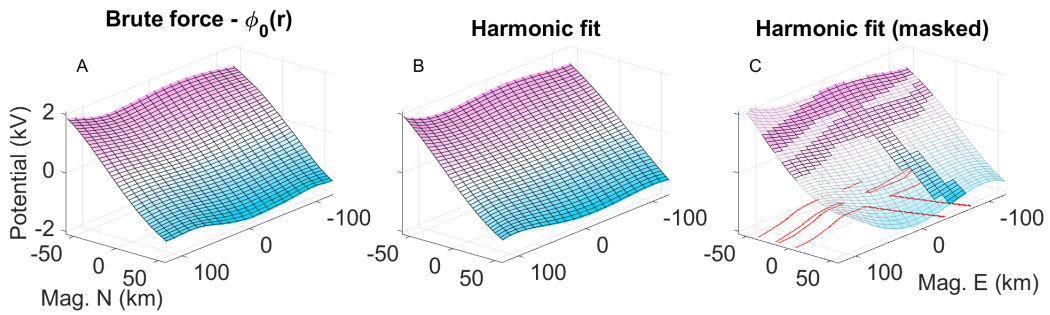


Figure 6. Validity of a harmonic function fit. **A:** Residual potential between brute force fitting and Eq. (21). **B:** Unmasked harmonic function fit from Eq. (24) with $m = 5$ and $q = 10$ m. **C:** Same as panel B but masked with the mask, \mathcal{M} , in red.

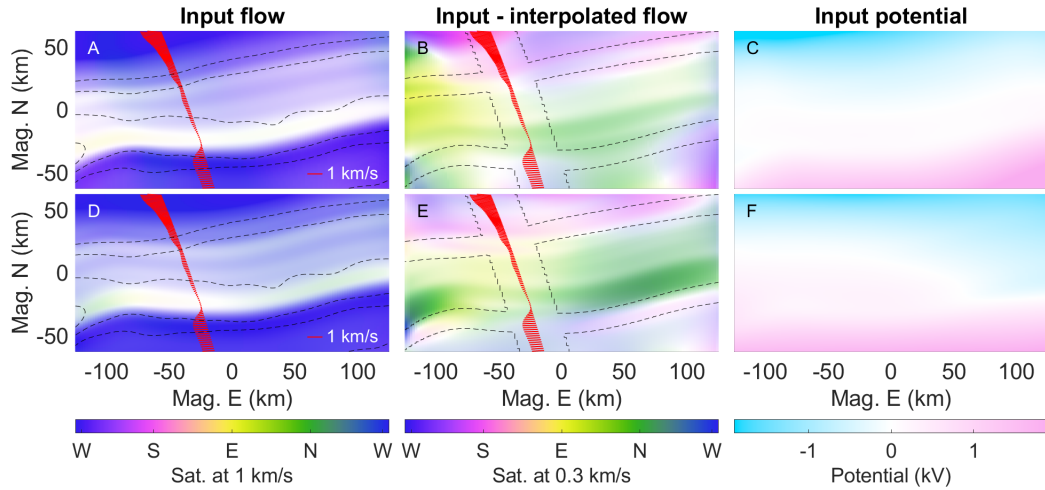


Figure 7. Input flow and potential maps used to drive simulations with (top row) and without (bottom row) replication scaling/rotating. **A, D:** Hue-saturation plots of $-\nabla\phi_c$ with contour lines of Σ_P . **B, E:** Flow error, i.e. $-\nabla\phi_c - \mathbf{v}_{\text{arc}}$, with masking contours where the harmonic function is fit. **C, F:** Input potential maps, ϕ_c .

flow remains westward resulting in a changing angle between the electric field and the conductance gradients. This has physical effects on auroral current closure (see Eq. (1)).

Comment on qualitative performance.

2.3 Weighted replications

In the event of a conjunction between auroral imagery and two flow data tracks, the replication method can simply be repeated up to the interpolation step. Both replications use the same primary and secondary boundaries as well as the same background flow, \mathbf{v}_{bg} . This background flow is determined by whichever replication is done first. The flow data smoothing is also performed with approximately equal Gaussian filter physical window widths.

Once both tracks have their replication and subsequent interpolated flow fields, they are weighted average with the weighting functions

$$w_A(\mathbf{r}) = \frac{1}{2} \left[1 + \tanh \left(\frac{d_{\min,B}(\mathbf{r}) - d_{\min,A}(\mathbf{r})}{s_w} \right) \right], \text{ and } w_B(\mathbf{r}) = 1 - w_A(\mathbf{r}). \quad (27)$$

Here, $d_{\min,A}$ is a map of the shortest straight-line distances from points \mathbf{r} to track A and similarly for track B . This configuration of weighting allows for two intersecting tracks. The scale length, s_w , will introduce flow gradients and has to be chosen with care. From here we have a new interpolated arc-disturbed plasma flow,

$$\mathbf{v}_{\text{arc}}(\mathbf{r}) = w_A(\mathbf{r})\mathbf{v}_{\text{arc},A}(\mathbf{r}) + w_B(\mathbf{r})\mathbf{v}_{\text{arc},B}(\mathbf{r}), \quad (28)$$

from which the methodology from Section 2.2.3 takes over. This ensures electrostatics, but it should be mentioned that, on top of the divergences still remaining in either track's interpolated field, this weighting function introduces additional divergence of the form

$$(\nabla \cdot \mathbf{v}_{\text{arc}})_w = \nabla w_A(\mathbf{r}) \cdot (\mathbf{v}_{\text{arc},A} - \mathbf{v}_{\text{arc},B}). \quad (29)$$

This weighting function, however, has small northward gradients and the interpolated flows are expected to not vary much eastward, i.e. ∇w_A is approximately orthogonal to

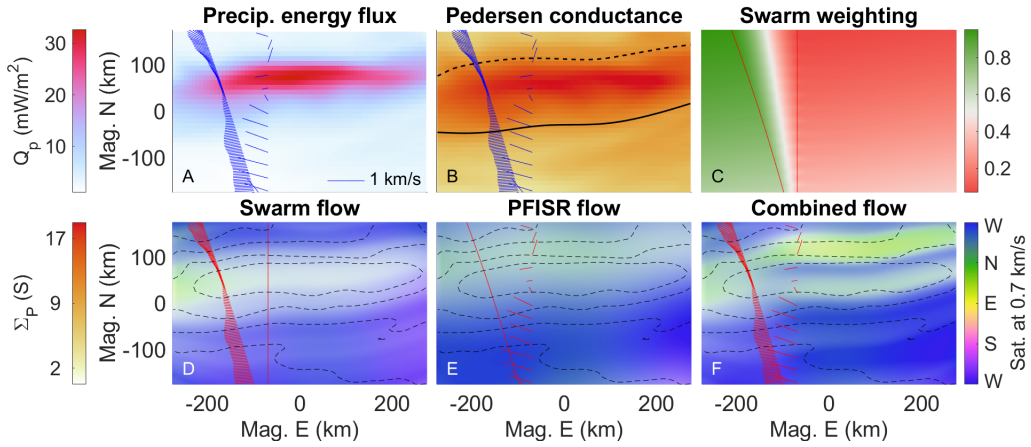


Figure 8. Weighted replication example. **A:** Precipitating total electron energy flux with plasma flow data from Swarm (left trajectory) and PFISR (right track) in blue. **B:** The GLOW derived Pedersen conductance with the primary (solid) and secondary (dashed) boundaries overlaid. **C:** The weighting map, w_A , used for the Swarm data with a scale length of $s_w = 200$ km. **D-F:** Resulting flow maps from using only Swarm data, only PFISR data, and from using both datasets, respectively.

349 $\mathbf{v}_{\text{arc},A} - \mathbf{v}_{\text{arc},B}$ resulting in minimal diverging flow. This ensures that the Helmholtz de-
 350 composition provides an electrostatic solution of the final flow map that doesn't stray
 351 far from the interpolated flow map.

352 For more than two replications the weighting function requires some adjustments,
 353 but this is also perfectly possible.

354 2.3.1 Weighted replication example

355 To illustrate the double replication methodology, a conjunction from the *Swarm-over-Poker-2023* campaign is used (Feb - March 2023, Poker Flat Research Range, AK).
 356 This campaign facilitated conjunctions of (among a variety of other data) ion flow data
 357 from the Thermal Ion Imagers (Knudsen et al., 2017) on ESA's Swarm mission, convec-
 358 tion flow data from AMISR's Poker Flat Incoherent Scatter Radar (PFISR) (Kelly &
 359 Heinselman, 2009; Nicolls & Heinselman, 2007; Heinselman & Nicolls, 2008), and multi-
 360 spectral, all-sky imagery from the Poker Flat DASC [dasc data ref](#). This campaign has
 361 developed a growing collection of heterogeneous auroral observations for the winter months
 362 of 2023. Our example uses data from March 19 at 8:23:44 UT (20.5 MLT).

364 Figure 8A summarizes this event showing a $Q_p \approx 30$ mW/m² (with $E_p \approx 7$ keV,
 365 not shown) auroral arc with some along-arc structure. The left trajectory shows flow data
 366 from Swarm B and the right track shows that from PFISR. Panel B also shows the Ped-
 367 ersen conductance (this time derived using GLOW (Solomon, 2017)) which is used to
 368 determine the arc boundaries and panel C shows the the weighting function used for the
 369 Swarm data. The bottom row gives the final continuous plasma flow maps when using
 370 only the Swarm data, or the PFISR data, or both. The individual reconstructions are
 371 dissimilar, but this is to be expected given the along-arc structure. [Note about how swarm](#)
 372 [B data was constructed \(ask Alex\).](#)

3 Driving GEMINI with the Replication Method

374 3.1 The GEMINI model

375 To investigate the effects of continuous plasma flow maps in conjunction with au-
 376 roral precipitation, we use state-of-the-art 3D ionospheric simulations provided by the
 377 Geospace Environment Model of Ion-Neutral Interactions (GEMINI) (M. D. Zettergren
 378 & Semeter, 2012; M. Zettergren & Snively, 2019). This is a multi-fluid (6 ions + elec-
 379 trons), quasi-electrostatic model with its particle continuity consisting of chemical pro-
 380 duction/loss and photo/impact ionization. Calculations of local densities, plasma flows,
 381 and temperatures are treated self-consistently and the model includes thermal con-
 382 duction heat flux, collisional heating, thermoelectric electron heat flux, and inelastic cool-
 383 ing/heating from photoelectrons. This is supplemented with Maxwell's equations and,
 384 at the time of writing, includes no displacement current or magnetic induction effects.
 385 With this, the system is solved through enforcing divergence-less currents, curl-free elec-
 386 tric fields, and invoking Ohm's law. Note: coming this fall: adaptive mesh refinement
 387 and neutral coupling!

388 3.2 Simulation examples

389 Figure 9 depicts GEMINI output data with Figure 7C as the flow driver and the
 390 same precipitation data used by example “c5” from Clayton et al. (2021). The calculated
 391 topside FAC slice is taken at an altitude of 200 km, but is translated down to 80 km for
 392 visualization purposes. In order to visualize FAC closure, we opt for current flux tubes
 393 which are made possible by the enforced condition of $\nabla \cdot \mathbf{j} = 0$ and the use of stream-
 394 lines sourced at closed elliptical curves (solid black curves). This enables an intuitive in-
 395 terpretation of auroral current closure by showing where a patch of FAC joins back with
 396 the magnetosphere or where a region of Hall current ends up. The dotted black and blue
 397 curves show the projection of the terminating ends of the flux tubes onto the FAC map.
 398 The green flux tube (28.4 kA) is a stereotypical example of FAC closure via the Peders-
 399 sen layer, closing down between 118 - 154 km. The orange tube (XX kA) runs under-
 400 neath it and shows exchange between a region of Hall current and Pedersen current up
 401 near the bottom of the Pedersen layer. This tube spans between 87 - 105 km in altitude
 402 at its lowest point, and exits the equatorward wall between 101 - 138 km. The red flux
 403 tube (23.9 kA) is, to some extent, a combination of these two, and has two exit regions.
 404 When this tube has its sourced downward FAC run out of upward FAC to close through
 405 in its paired sheet, it continues onto the next upward FAC sheet poleward of it where
 406 the remaining XX kA is closed.

407 To show the effects of steps 2 and 3 of section 2.2.2, the output from Figure 9 is
 408 also simulated with the same precipitation maps, but with the replication scaling and
 409 rotating turned off (see Figure 7D-F). Figure 10 divides the topside FAC maps of both
 410 simulations into the three terms from Eq. (1) in order to look at the effects of the plasma
 411 flow shear and precipitation gradients separately. Figure 10D shows sensible results given
 412 a single arc boundary, but panels E and F illustrate an amalgamation of two apparent
 413 arc profiles at the poleward edge of the arc. The rotation between the arc disturbed elec-
 414 tric field and the Pedersen and Hall conductance gradients causes the secondary bound-
 415 ary to substantiate through, even though these replications are fully transparent to this
 416 second boundary.

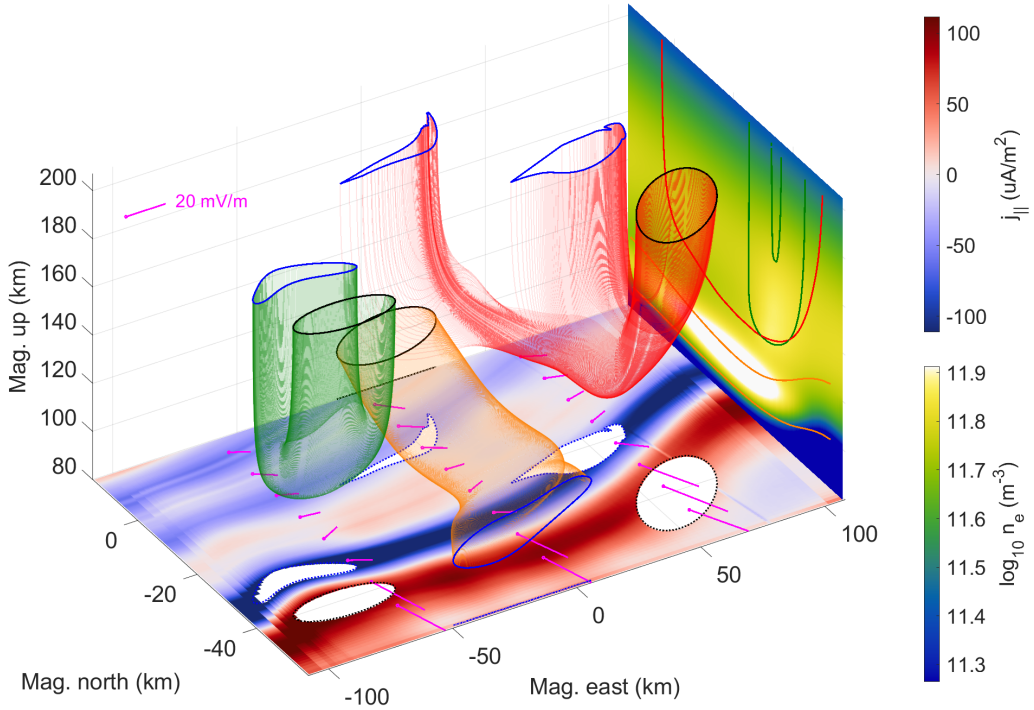


Figure 9. Plasma flow driven GEMINI output with input from the potential in Figure 7C. Current flux tubes are colored for distinction purposes and start/end at solid black/blue curves. The orange flux tube runs in reverse. **East side:** A north-up slice of electron density taken at 0 km east along with flux tube outline projections. **Bottom side:** An east-north slice of FAC (with parallel being down) taken at 200 km altitude along with flux tube start/end curve projections and electric field vectors (magenta). Note that these vectors include the background electric field.

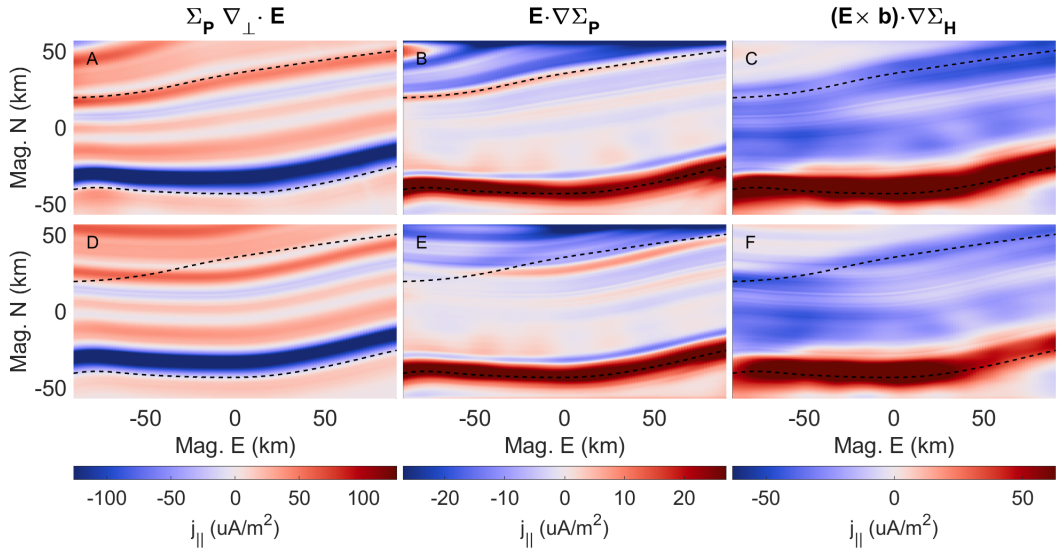


Figure 10. Calculated FAC components from Eq. (1). **A-C:** Terms 1 through 3 respectively split from the FAC map shown in Figure 9 along with arc boundaries (dashed). **D-E:** Same as the top row but with replication scaling and rotating turned off.

417 **4 Discussions**

418 **Why do we need 3D simulations?** Figure 9 indicates that even for one of the most
 419 basic examples of an auroral arc system, the morphology of current closure is 3D in nature.
 420 The green flux tubes depicts a more instinctive auroral current closure type using
 421 largely Pedersen currents to close (Mallinckrodt, 1985), however, the red flux tube illus-
 422 trates a less common view of FAC current closure; not all current from one FAC sheet
 423 has to close with its neighbouring sheet. This tube “digs” deeper into the Hall layer, sub-
 424 sequentially rotating, in search of another closure path. Secondly, the orange flux tube is
 425 mostly Hall current, but includes divergence, i.e. the last term in Eq. (1), being fed into
 426 Pedersen currents as the tube climbs to reach higher conductivity (see the electron den-
 427 sity panel). This Pedersen current can no longer be used to close FACs, which is how
 428 diverging Hall currents can indirectly effect j_{\parallel} . Additionally, FAC closure is not restricted
 429 to the Pedersen or Hall layers at around 90 - 130 km; depending on the perpendicular
 430 distance from the FAC sheet inflection line, FACs can close as high as 144 km.

431 To better understand quasistatic auroral arc scale science, and the non-passive role
 432 the ionosphere plays in MI coupling, these 3D features require further studies. This re-
 433 quires 3D auroral simulations and, in turn, electrostatic, continuous, 2D, topside F-region
 434 boundary maps.

435 **How have we improved 2D auroral arc drivers?** We have developed techniques for
 436 creating such maps which focus on auroral physical and gradient scale lengths, and dis-
 437 crete sheet-like morphologies. [sentence about reconstruction](#). The replication method-
 438 ology aims to use maximal information from the 2D precipitation maps to get the most
 439 intuitive plasma flow map possible. To do so, and as improvements to work done by (Clayton
 440 et al., 2019), we use:

- 441 1. imagery derived Pedersen conductance contour lines, in place of energy flux gra-
 442 dient, as a more natural choice for copying electric field data
- 443 2. a secondary auroral arc boundary to which the plasma flow data is scaled in an
 444 attempt to co-locate shorted-out electric fields with enhanced precipitation
- 445 3. plasma flow rotation to ensure the zeroth order electric field shock definition of
 446 auroral arcs

447 Figure 7 and 10 demonstrate these improvements. These additional measures ensure that
 448 the directions of the electric fields and the image related gradients are more intuitive,
 449 and they are the next step towards studying auroral arcs that stray from their ideal, sheet-
 450 like morphologies.

451 **Cautionary remarks.**

452 **CAUTIONARY REMARKS. WHAT TO WATCH OUT FOR**

- 453 - it is important to match flow and imagery to low order assumptions (marghitu)
- 454 - Fg8: v/SigmaP/H need consistent smoothing so divE balance w/ gradSigma
- 455 - too much flow shear mean FAC has no geophysical closure paths
- 456 - runs are limited due to poor resolution of image inversion, but see alex work
- 457 - interpolating scattered flow needs bicubic to avoid stepwise first derivatives
- 458 - need continuity of C^1 or higher
- 459 - bilinear interpolation can result in a strong rippling of simulated fac

460 **WHERE WILL WE GO FROM HERE?**

- 461 - make public catalog to address motivation of paper Section 1.1
- 462 - Q1: "What self-consistency constraints exist in creating a geophysically coherent
- 463 set of F-region quasistatic auroral system drivers?"
- 464 - Q2: "What understanding of auroral system science can be gained by investigating
- 465 the 3D morphology of ionospheric current closure?"
- 466 - Q3: "What degree of along-arc structure significantly breaks the sheetlike discrete
- 467 auroral model and what auroral features are most sensitive to this structure?"
- 468 - add to catalog of hand picked collection of swop data driven runs
- 469 - add to catalog idealized simulations
- 470 - compare data driven runs against data inspired catalog to see what's what
- 471 - publish infrastructure for running replications and ideal for catalog
- 472 - improve replication by having flow following contour lines (no boundaries)
- 473 - eiscat3d will provide a 2D array of flows
- 474 - merge with lompe

475 **5 Conclusions**

- 476 1. Even for the most basic auroral systems, a 2D description hides the 3D nature of
477 current closure.
- 478 2. The 3D auroral system morphology caused by the interplay between current, con-
479 ductivity, and plasma flow sets self consistency restrictions on the natural scale
480 lengths of arcs.
- 481 3. When extrapolating plasma flow data surrounding auroral arcs, it is important
482 to scale and rotate the data in accordance with conductance morphology.
- 483 4. When data driving 3D auroral simulations, proper interpolation and model res-
484 olution are crucial.

485 talk about the next paper, catalog, ready set go

486 **Open Research Section**

487 This section MUST contain a statement that describes where the data support-
488 ing the conclusions can be obtained. Data cannot be listed as "Available from authors"
489 or stored solely in supporting information. Citations to archived data should be included
490 in your reference list. Wiley will publish it as a separate section on the paper's page. Ex-
491 amples and complete information are here: [https://www.agu.org/PublishwithAGU/
492 Publish/AuthorResources/Data for Authors](https://www.agu.org/PublishwithAGU/Publish/AuthorResources/DataforAuthors)

493 **Acknowledgments**

494 The Poker Flat Incoherent Scatter Radar is operated by the SRI International for the
495 National Science Foundation as part of the AMISR program through cooperative agree-
496 ment AGS-1840962. AMISR data are available at <https://data.amisr.com/database/>.
497 NSF CEDAR SoP2023, GEMINI grants, FINESST grant, NASA HEC if we use it, isin-
498 glass grant? arcs grant?

499 **References**

- 500 Ahlfors, L. V. (1953). Complex analysis: an introduction to the theory of analytic
501 functions of one complex variable. *New York, London, 177.*
- 502 Amm, O. (1997). Ionospheric elementary current systems in spherical coordinates
503 and their application. *Journal of geomagnetism and geoelectricity*, 49(7), 947-
504 955. doi: 10.5636/jgg.49.947
- 505 Bristow, W. A., Hampton, D. L., & Otto, A. (2016). High-spatial-resolution velocity
506 measurements derived using Local Divergence-Free Fitting of SuperDARN
507 observations. *Journal of Geophysical Research: Space Physics*, 121(2), 1349-
508 1361. Retrieved from <https://agupubs.onlinelibrary.wiley.com/doi/abs/10.1002/2015JA021862> doi: <https://doi.org/10.1002/2015JA021862>
- 509 Clayton, R., Burleigh, M., Lynch, K. A., Zettergren, M., Evans, T., Grubbs, G., ...
510 Varney, R. (2021). Examining the auroral ionosphere in three dimensions using
511 reconstructed 2D maps of auroral data to drive the 3D GEMINI model. *Jour-
512 nal of Geophysical Research: Space Physics*, 126(11). Retrieved from <https://agupubs.onlinelibrary.wiley.com/doi/abs/10.1029/2021JA029749> doi:
513 <https://doi.org/10.1029/2021JA029749>
- 514 Clayton, R., Lynch, K., Zettergren, M., Burleigh, M., Conde, M., Grubbs, G., ...
515 Varney, R. (2019). Two-dimensional maps of in situ ionospheric plasma
516 flow data near auroral arcs using auroral imagery. *Journal of Geophys-
517 ical Research: Space Physics*, 124(4), 3036-3056. Retrieved from <https://agupubs.onlinelibrary.wiley.com/doi/abs/10.1029/2018JA026440> doi:
518 <https://doi.org/10.1029/2018JA026440>

- 522 Cowley, S. W. H. (2000). Magnetosphere-ionosphere interactions: A tutorial review.
 523 *Magnetospheric Current Systems, Geophysical Monograph Series, 118*, 91-106.
- 524 Enengl, F., Kotova, D., Jin, Y., Clausen, L. B. N., & Miloch, W. J. (2023). Ionospheric plasma structuring in relation to auroral particle precipitation. *J. Space Weather Space Clim., 13*. Retrieved from <https://doi.org/10.1051/swsc/2022038> doi: 10.1051/swsc/2022038
- 528 Erlandson, R., Lynch, K. A., Samara, M., Anderson, B., Bortnik, J., Burleigh, M., ...
 529 Zou, S. (2024). *Auroral Reconstruction CubeSwarm (ARCS)*. (Manuscript in
 530 Preperation)
- 531 Fang, X., Randall, C. E., Lummerzheim, D., Solomon, S. C., Mills, M. J., Marsh,
 532 D. R., ... Lu, G. (2008). Electron impact ionization: A new parameterization
 533 for 100 ev to 1 mev electrons. *Journal of Geophysical Research: Space Physics,*
 534 113(A9). Retrieved from <https://agupubs.onlinelibrary.wiley.com/doi/abs/10.1029/2008JA013384> doi: <https://doi.org/10.1029/2008JA013384>
- 536 Fang, X., Randall, C. E., Lummerzheim, D., Wang, W., Lu, G., Solomon, S. C., &
 537 Frahm, R. A. (2010). Parameterization of monoenergetic electron impact
 538 ionization. *Geophysical Research Letters, 37*(22). Retrieved from <https://agupubs.onlinelibrary.wiley.com/doi/abs/10.1029/2010GL045406> doi:
 540 <https://doi.org/10.1029/2010GL045406>
- 541 Fujii, R., Amm, O., Vanhamäki, H., Yoshikawa, A., & Ieda, A. (2012, 11).
 542 An application of the finite length cowling channel model to auroral arcs
 543 with longitudinal variations. *Journal of Geophysical Research, 117*. doi:
 544 10.1029/2012JA017953
- 545 Fujii, R., Amm, O., Yoshikawa, A., Ieda, A., & Vanhamäki, H. (2011). Re-
 546 formulation and energy flow of the Cowling channel. *Journal of Geo-
 547 physical Research: Space Physics, 116*(A2). Retrieved from <https://agupubs.onlinelibrary.wiley.com/doi/abs/10.1029/2010JA015989> doi:
 549 <https://doi.org/10.1029/2010JA015989>
- 550 Heinselman, C. J., & Nicolls, M. J. (2008). A Bayesian approach to electric field
 551 and E-region neutral wind estimation with the Poker Flat Advanced Modular
 552 Incoherent Scatter Radar. *Radio Science, 43*(5). Retrieved from <https://agupubs.onlinelibrary.wiley.com/doi/abs/10.1029/2007RS003805> doi:
 554 <https://doi.org/10.1029/2007RS003805>
- 555 Kamide, Y., Richmond, A. D., & Matsushita, S. (1981). Estimation of ionospheric
 556 electric fields, ionospheric currents, and field-aligned currents from ground
 557 magnetic records. *Journal of Geophysical Research: Space Physics, 86*(A2),
 558 801-813. Retrieved from <https://agupubs.onlinelibrary.wiley.com/doi/abs/10.1029/JA086iA02p00801> doi: <https://doi.org/10.1029/JA086iA02p00801>
- 561 Kelley, M. C. (2009). *The Earth's ionosphere: plasma physics and electrodynamics*
 562 (2nd ed.). Amsterdam, Netherlands: Academic Press.
- 563 Kelly, J., & Heinselman, C. (2009). Initial results from Poker Flat Incoherent Scatter
 564 Radar (PFISR). *Journal of Atmospheric and Solar-Terrestrial Physics,*
 565 71(6), 635. Retrieved from <https://www.sciencedirect.com/science/article/pii/S1364682609000121> (Advances in high latitude upper atmospheric science with the Poker Flat Incoherent Scatter Radar (PFISR)) doi:
 568 <https://doi.org/10.1016/j.jastp.2009.01.009>
- 569 Khazanov, G. V., Robinson, R. M., Zesta, E., Sibeck, D. G., Chu, M., & Grubbs,
 570 G. A. (2018). Impact of precipitating electrons and magnetosphere-ionosphere
 571 coupling processes on ionospheric conductance. *Space Weather, 16*(7), 829-
 572 837. Retrieved from <https://agupubs.onlinelibrary.wiley.com/doi/abs/10.1029/2018SW001837> doi: <https://doi.org/10.1029/2018SW001837>
- 574 Knudsen, D. J., Burchill, J. K., Buchert, S. C., Eriksson, A. I., Gill, R., Wahlund,
 575 J.-E., ... Moffat, B. (2017). Thermal ion imagers and langmuir probes
 576 in the Swarm electric field instruments. *Journal of Geophysical Re-*

- 577 *search: Space Physics, 122(2), 2655-2673.* Retrieved from <https://agupubs.onlinelibrary.wiley.com/doi/abs/10.1002/2016JA022571> doi:
 578 <https://doi.org/10.1002/2016JA022571>
- 579 Laundal, K. M., Reistad, J. P., Hatch, S. M., Madelaire, M., Walker, S., Hovland,
 580 A. Ø., ... Sorathia, K. A. (2022). Local mapping of polar ionospheric electro-
 581 dynamics. *Journal of Geophysical Research: Space Physics, 127(5)*. Retrieved
 582 from <https://agupubs.onlinelibrary.wiley.com/doi/abs/10.1029/2022JA030356> doi: <https://doi.org/10.1029/2022JA030356>
- 583 Lotko, W. (2004). Inductive magnetosphere-ionosphere coupling. *Journal
 584 of Atmospheric and Solar-Terrestrial Physics, 66(15)*, 1443-1456. Retrieved
 585 from <https://www.sciencedirect.com/science/article/pii/S1364682604001518> doi: <https://doi.org/10.1016/j.jastp.2004.03.027>
- 586 Lynch, K. A., Erlandson, R., Samara, M., Anderson, B., Bortnik, J., Burleigh, M., ...
 587 Zou, S. (2024). *Auroral Reconstruction CubeSwarm (ARCS)*. (Manuscript in
 588 Preparation)
- 589 Lynch, K. A., McManus, E., Gutow, J., Burleigh, M., & Zettergren, M. (2022). An
 590 ionospheric conductance gradient driver for subauroral picket fence visible sig-
 591 natures near STEVE events. *Journal of Geophysical Research: Space Physics, 127(12)*. Retrieved from <https://agupubs.onlinelibrary.wiley.com/doi/abs/10.1029/2022JA030863> doi: <https://doi.org/10.1029/2022JA030863>
- 592 Mallinckrodt, A. J. (1985). A numerical simulation of auroral ionospheric electro-
 593 dynamics. *Journal of Geophysical Research: Space Physics, 90(A1)*, 409-417.
 594 Retrieved from <https://agupubs.onlinelibrary.wiley.com/doi/abs/10.1029/JA090iA01p00409> doi: <https://doi.org/10.1029/JA090iA01p00409>
- 595 Marghitu, O. (2012). Auroral arc electrodynamics: Review and outlook. *Rela-
 596 tionship between auroral phenomenology and magnetospheric processes: Earth and
 597 other planets, Geophysical Monograph Series, 197*, 143-158.
- 598 Mule, A. (2023, October 1). Personal communication.
- 599 Mule, A. (2024, February 8). Personal communication.
- 600 Nicolls, M. J., Cosgrove, R., & Bahcivan, H. (2014). Estimating the vector
 601 electric field using monostatic, multibeam incoherent scatter radar mea-
 602 surements. *Radio Science, 49(11)*, 1124-1139. Retrieved from <https://agupubs.onlinelibrary.wiley.com/doi/abs/10.1002/2014RS005519> doi:
 603 <https://doi.org/10.1002/2014RS005519>
- 604 Nicolls, M. J., & Heinselman, C. J. (2007). Three-dimensional measurements
 605 of traveling ionospheric disturbances with the Poker Flat Incoherent Scatter Radar. *Geophysical Research Letters, 34(21)*. Retrieved from <https://agupubs.onlinelibrary.wiley.com/doi/abs/10.1029/2007GL031506> doi:
 606 <https://doi.org/10.1029/2007GL031506>
- 607 Richmond, A. D., & Kamide, Y. (1988). Mapping electrodynamic features of
 608 the high-latitude ionosphere from localized observations: Technique. *Jour-
 609 nal of Geophysical Research: Space Physics, 93(A6)*, 5741-5759. Retrieved
 610 from <https://agupubs.onlinelibrary.wiley.com/doi/abs/10.1029/JA093iA06p05741> doi: <https://doi.org/10.1029/JA093iA06p05741>
- 611 Robinson, R. M., Vondrak, R. R., Miller, K., Dabbs, T., & Hardy, D. (1987). On
 612 calculating ionospheric conductances from the flux and energy of precipitating
 613 electrons. *Journal of Geophysical Research: Space Physics, 92(A3)*, 2565-
 614 2569. Retrieved from <https://agupubs.onlinelibrary.wiley.com/doi/abs/10.1029/JA092iA03p02565> doi: <https://doi.org/10.1029/JA092iA03p02565>
- 615 Ruohoniemi, J. M., Greenwald, R. A., Baker, K. B., Villain, J. P., Hanuise, C., &
 616 Kelly, J. (1989). Mapping high-latitude plasma convection with coherent HF
 617 radars. *Journal of Geophysical Research: Space Physics, 94(A10)*, 13463-13477.
 618 Retrieved from <https://agupubs.onlinelibrary.wiley.com/doi/abs/10.1029/JA094iA10p13463> doi: <https://doi.org/10.1029/JA094iA10p13463>
- 619 Seyler, C. E. (1990). A mathematical model of the structure and evolu-

- 632 tation of small-scale discrete auroral arcs. *Journal of Geophysical Re-*
 633 *search: Space Physics*, 95(A10), 17199-17215. Retrieved from <https://agupubs.onlinelibrary.wiley.com/doi/abs/10.1029/JA095iA10p17199>
 634 doi: <https://doi.org/10.1029/JA095iA10p17199>
- 635 Sobel, I. (2014, 02). An isotropic 3x3 image gradient operator. *Presentation at Stan-*
 636 *ford A.I. Project 1968.*
- 637 Solomon, S. C. (2017). Global modeling of thermospheric airglow in the far ultra-
 638 violet. *Journal of Geophysical Research: Space Physics*, 122(7), 7834-7848.
 639 Retrieved from <https://agupubs.onlinelibrary.wiley.com/doi/abs/10.1002/2017JA024314> doi: <https://doi.org/10.1002/2017JA024314>
- 640 Wang, X., Cai, L., Aikio, A., Vanhamäki, H., Virtanen, I., Zhang, Y., ... Liu,
 641 S. (2024). Ionospheric conductances due to electron and ion precipita-
 642 tions: A comparison between EISCAT and DMSP estimates. *Journal of*
 643 *Geophysical Research: Space Physics*, 129(2). Retrieved from <https://agupubs.onlinelibrary.wiley.com/doi/abs/10.1029/2023JA032354> doi:
 644 <https://doi.org/10.1029/2023JA032354>
- 645 Wolf, R. A. (1975, Mar 01). Ionosphere-magnetosphere coupling. *Space Science Re-*
 646 *views*, 17(2), 537-562. Retrieved from <https://doi.org/10.1007/BF00718584>
 647 doi: 10.1007/BF00718584
- 648 Yano, Y., & Ebihara, Y. (2021). Three-dimensional closure of field-aligned cur-
 649 rents in the polar ionosphere. *Journal of Geophysical Research: Space Physics*,
 650 126(9). Retrieved from <https://agupubs.onlinelibrary.wiley.com/doi/abs/10.1029/2021JA029421> doi: <https://doi.org/10.1029/2021JA029421>
- 651 Zettergren, M., & Snively, J. (2019). Latitude and longitude dependence of iono-
 652 spheric TEC and magnetic perturbations from infrasonic-acoustic waves gener-
 653 ated by strong seismic events. *Geophysical Research Letters*, 46(3), 1132-1140.
 654 doi: 10.1029/2018GL081569
- 655 Zettergren, M. D., & Semeter, J. L. (2012). Ionospheric plasma transport and
 656 loss in auroral downward current regions. *Journal of Geophysical Research:*
 657 *Space Physics*, 117(A6). Retrieved from <https://agupubs.onlinelibrary.wiley.com/doi/abs/10.1029/2012JA017637> doi: <https://doi.org/10.1029/2012JA017637>
- 658
- 659
- 660
- 661
- 662
- 663